NISTIR 5268

Research for Electric Energy Systems - An Annual Report

William E. Anderson
Editor

U.S. DEPARTMENT OF COMMERCE
Technology Administration
National Institute of Standards
and Technology
Electronics and Electrical Engineering Laboratory
Electricity Division
Gaithersburg, MD 20899

Prepared for
Department of Energy
Division of Electric Energy Systems
1000 Independence Avenue, SW
Washington, DC 20585

NIST

NISTIR 5268

Research for Electric Energy Systems - An Annual Report

William E. Anderson
Editor

U.S. DEPARTMENT OF COMMERCE
Technology Administration
National Institute of Standards
and Technology
Electronics and Electrical Engineering Laboratory
Electricity Division
Gaithersburg, MD 20899

Prepared for
Department of Energy
Division of Electric Energy Systems
1000 Independence Avenue, SW
Washington, DC 20585

December 1992

Issued October 1993

U.S. DEPARTMENT OF COMMERCE
Ronald H. Brown, Secretary

TECHNOLOGY ADMINISTRATION
Mary L. Good, Under Secretary for Technology

NATIONAL INSTITUTE OF STANDARDS AND TECHNOLOGY
Arati Prabhakar, Director

Foreword

This report summarizes the progress of two technical investigations conducted during CY 92. Although reasonable efforts have been made to ensure the reliability of the data presented, it must be emphasized that this is an interim progress report and that further experimentation and analysis may be performed before the conclusions from any of these investigations are formally published. It is therefore possible that some of the observations presented in this report will be modified, expanded, or clarified by our subsequent research[1].

[1]The identification of commercial materials and their sources is made to describe the experiment adequately. In no case does this identification imply recommendation by the National Institute of Standards and Technology, nor does it imply that the product is the best available.

Table of Contents

Research for Electric Energy Systems – An Annual Report

William E. Anderson, Editor

Abstract

This report documents the technical progress in the two investigations which make up the project "Support of Research Projects for Electrical Energy Systems," Department of Energy Task Order Number 137, funded by the U.S. Department of Energy and performed by the Electricity Division of the National Institute of Standards and Technology (NIST). The first investigation is concerned with the measurement of magnetic fields in support of epidemiogical and *in vitro* studies of biological field effects. During 1992, the derivation of equations which predict differences between the average magnetic flux density using circular coil probes and the flux density at the center of the probe, assuming a dipole magnetic field, were completed. The information gained using these equations allows the determination of measurement uncertainty due to probe size when magnetic fields from many electrical appliances are characterized. Consultations with various state and federal organizations and the development of standards related to electric and magnetic field measurements continued. The second investigation is concerned with two different activities related to compressed-gas insulated high voltage systems: 1) the measurement of dissociative electron attachment cross sections and negative ion production in S_2F_{10}, S_2OF_{10}, and $S_2O_2F_{10}$, and 2) Monte-Carlo simulations of ac-generated partial-discharge pulses that can occur in SF_6-insulated power systems and can be sources of gas decomposition.

1 NIST FIELDS PROJECT

Task 01
Martin Misakian
Electricity Division
National Institute of Standards and Technology

1.1 Introduction

The objectives of this project are to develop methods to evaluate and calibrate instruments which are used, or are being developed, to characterize electrical parameters in the vicinity of power lines and in laboratory apparatus designed to simulate the power line environment. The characterization of extremely low frequency (ELF) electric and magnetic fields (EMFs) in environments away from power lines, e.g., in residences, the work place, and in transportation systems, is also considered. Electrical measurement support is provided to the Department of Energy (DOE) via site visits to laboratories where EMF research is conducted with support from DOE (similar support is provided to the Electric Power Research Institute at cost).

During 1992, the derivation of equations which predict differences between the average magnetic flux density using circular coil probes and the flux density at the center of the probe, assuming a dipole magnetic field, were completed. The information gained using these equations allows the determination of measurement uncertainty due to probe size when magnetic fields from many electrical appliances are characterized. A draft manuscript has been prepared and will be submitted to the NIST Journal of Research in 1993. Portions of the paper are reproduced below.

Other activities related to the NIST Fields Project during 1992 included numerous consultations and collaborations with other government agencies, committees in professional societies, and research groups. A tabulation of some of these activities is given in the next section.

1.2 Consultations and Collaborations

The NIST Fields Project activities in 1992 included:

(a) Site visits to the University of Rochester on behalf of DOE, and the University of Kentucky on behalf of the Electric Power Research Institute (EPRI), during which there were consultations on measurements of fields, and measurements of magnetic fields in exposure systems. Reports describing the measurement results were sent to the sponsoring agencies.

(b) Participation in an advisory panel meeting for the National Cancer Institute (NCI) childhood cancer study. This study is making steady progress and is scheduled for completion in late 1994 or early 1995.

(c) Participation in the DOE-sponsored EMF Science and Engineering Workshop during which needed research pertaining to the EMF health effects question was identified and prioritized.

(d) Continued consultation with the Food and Drug Administration (Rockville, MD) during balloting of a new IEEE standard which describes a measurement protocol for characterizing electric and magnetic fields from visual display terminals. A final draft of this standard should be completed in early 1993.

(e) Preparation of a manuscript, in collaboration with members of the AC Fields Working Group (IEEE Power Engineering Society), which describes a protocol for performing spot measurements of magnetic fields in residences. Because of the limitations associated with spot measurements, the protocol cannot become a standard. The abstract of the paper is reproduced here to outline the paper's content and to note the limitations associated with spot measurements.

"This paper describes a simple protocol for measuring power frequency magnetic fields in residences. The protocol should not be interpreted as an IEEE standard, but if followed, will provide a degree of procedural uniformity that currently does not exist. The measurement procedures are simple and not intended to characterize the temporal and spatial variability of magnetic field levels in residences. The protocol contains a structured component for measurements which are performed at specific locations, and an unstructured component for measurements which are performed at locations requested by the occupants. The protocol requires personnel performing the measurements to explain the metrology-related limitations associated with the measurement results. This paper also discusses terminology related to power frequency magnetic fields and their measurement, the meaning of measurement accuracy and variability within the context of residential magnetic field measurements, and examples of measurement approaches that characterize the variability of magnetic field levels."

The paper was presented by NIST at the 1992 IEEE Summer Power Engineering Society Meeting and will be published in the IEEE Transactions on Power Delivery in 1994.

(f) Participation in two meetings of The National Institutes of Health study sections during which research proposals related to EMF biological effects were evaluated.

(g) Completion of a primer manuscript for conducting *in vitro* bioeffects studies with ELF magnetic and electric fields. The manuscript was submitted to

the journal, Bioelectromagnetics, and has been accepted for publication as a special issue of the journal in 1993. The primer, which is the first of its kind, was prepared at NIST in collaboration with biologists and physicists at other research institutions. Primers of this type are called for in the National EMF Research and Communication Program.

(h) Acceptance of a task force leadership role (IEEE AC Fields Working Group) to prepare a new draft standard for electric and magnetic field instrumentation used to measure ELF magnetic and electric fields. "Zeroth" order and first drafts of the document were prepared at NIST in 1992 and circulated to members of the task force for comments. This project is expected to continue into 1994. NIST is also revising an existing IEEE standard (IEEE Std. 644–1987, IEEE Standard Procedures for Measurement of Power Frequency Electric and Magnetic Fields from AC Power Lines) in collaboration with the AC Fields Working Group.

(i) Reviews of draft reports from DOE (EMF Workshop and Research Plans), EPRI-Power Electronics Application Center, and the Oak Ridge Associated Universities Panel (for Committee on Interagency Radiation Research and Policy Coordination), and elements of proposals sent to the National Institute of Environmental Health Sciences (National Toxicology Program).

(j) Participation in interagency committee meetings at DOE focusing on coordination for EMF research.

(k) Participation in meetings of a new scientific advisory panel for bioeffects research with dc electric fields and ions at Hydro-Quebec.

(l) Renewed progress on completion of the National Council on Radiation Protection and Measurements report on ELF field effects which is being prepared by Scientific Committee 89–3. The draft report is expected to be completed in 1993.

(m) Participation in the final meeting of the planning committee organized by the Health Effects Institute (Cambridge, MA) to prepare a research plan for EMF research.

NIST also received recognition for its fields-related activities when M. Misakian was made a Senior Member of the IEEE, and accepted an invitation to become chairman of a new working group on ELF measurements (IEEE Standards Coordinating Committee 28–Subcommittee 1). M. Misakian also presented an invited paper at the EPRI-Power Electronics Application Center- sponsored "End-Use Magnetic Fields R & D Workshop," and was invited to present a talk on magnetic and electric field measurement methods at the 1993 IEEE Symposium on Electromagnetic Compatibility.

1.3 Coil Probe Dimensions and Uncertainties During Measurements of Nonuniform ELF Magnetic Fields

1.3.1 Introduction

The concern in the mid-1970s regarding health effects from exposure to electric and magnetic fields in the vicinity of power lines has shifted in recent years to health effect concerns from exposure to power frequency magnetic fields in residences, the work place, and in transportation systems [1–3]. The magnetic fields in these environments can be highly nonuniform, particularly near electrical equipment such as motors, transformers and heating elements. This report considers the difference between the calculated average magnetic flux density, B_{av}, as determined using magnetic field meters with single-axis and three-axis circular coil probes, and the calculated magnetic flux density at the center of the probes, B_o, assuming the field is produced by a small loop of alternating current, i.e., a magnetic dipole. The magnetic dipole field is chosen as the relevant field because to a good approximation its geometry simulates the field geometry of many electrical appliances and equipment [4]. The difference between B_{av} and B_o can be regarded as a source of measurement uncertainty because the center of the probe is normally considered the measurement location. While differences between B_{av} and B_o will be small in many situations, e.g., near ground level in the vicinity of power lines where the field changes slowly, the difference can become significant in the highly nonuniform magnetic fields close to electrical equipment.

In this report, two comparisons are made: (1) the maximum average magnetic field determined using a single-axis probe, B_{av1}, with B_o as a function of r/a where r is the distance between the magnetic dipole and the center of the probe, and a is the radius of the probe, and (2) the resultant magnetic field determined using a three-axis probe with B_o as a function of r/a. The resultant magnetic field, B_{av3}, is defined as [5]

$$B_{\mathrm{av3}} = \sqrt{B_1^2 + B_2^2 + B_3^2} \tag{1}$$

where B_1, B_2 and B_3 are average magnetic field components as measured by three orthogonally oriented coil probes.

Comparison (1) is made because maximum magnetic field values are sometimes measured, using single-axis field meters, to characterize the magnetic field [5, 6]. However, for a given value of r/a, it will be seen that the difference between B_{av1} and B_o will be a function of the orientation of the magnetic dipole relative to the probe. Because the relative orientation is not known during most measurements, what is of interest is the largest difference between B_{av1} and B_o for a given value of r/a. This largest difference will be designated ΔB_{max1}. The quantity ΔB_{max1} is determined in the following way. The single-axis probe is rotated for fixed values of r/a and the spherical coordinate, θ (Figure 1(a)), until the largest average magnetic field, B_{av1},

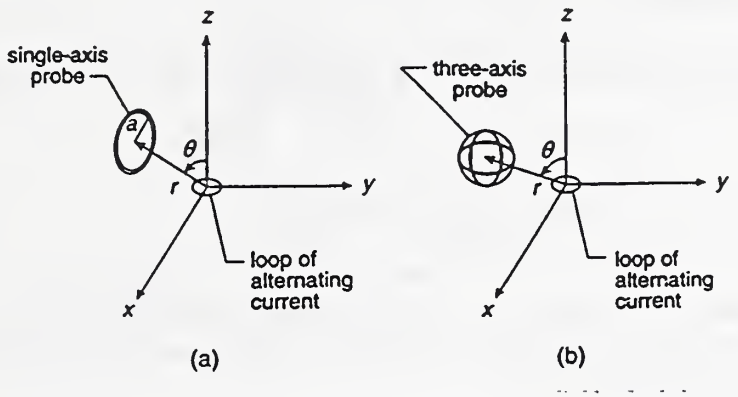

Figure 1. (a) Single-axis and (b) three-axis circular coil probes in dipole magnetic field produced by small loop of current.

is found. This value of B_{av1} is compared with the magnetic field at the center of the probe, B_o, and the difference is recorded. The orientation of the magnetic dipole with respect to the probe is then varied by moving the probe to another location while keeping r/a fixed, i.e., by changing θ in Figure 1(a). The probe is rotated again until the largest average magnetic field, B_{av1}, is found. B_{av1} is again compared with the magnetic field at the center of the probe, B_o, and the difference is recorded. This process is repeated for other dipole orientations (i.e., angle θ) until the largest difference, ΔB_{max1}, is found. An example of this process is shown in Section 1.3.5.

Comparison (2) is made as a three-axis probe is rotated about three axes parallel to the three Cartesian coordinates x, y, and z. The difference between B_{av3} and B_o will vary as a function of rotation angle, but what will be of interest again is the largest difference, ΔB_{max3}, for a given r/a. Also as for comparison (1), because the relative orientations of the magnetic dipole and the three-axis probe will be unknown in most measurement situations, B_{av3} will be examined as a function of r/a and the spherical coordinate, θ, in order to determine the largest difference, ΔB_{max3}.

1.3.2 Expressions for Average Magnetic Flux Density

In the derivations given below, it is assumed that the cross sectional area of the wire in the coil probes and the opposing magnetic field produced by current induced in the probes are negligible. In addition, we assume for the three-axis probe that the three orthogonally oriented coils have circular cross sections of equal area. These

assumptions either can be met in practice or can be taken into account via a calibration process.

1.3.3 Single-Axis Probe

The average magnetic flux density, B_{av}, for a single coil probe with cross-sectional area A is given by

$$B_{\text{av}} = \frac{1}{A} \int \int_A \vec{B} \cdot \hat{n}\, dA, \tag{2}$$

where dA is an element of probe area, $\hat{n}$ is a unit vector perpendicular to A, and $\vec{B}$ is the magnetic flux density. In spherical coordinates, the magnetic flux density for a small current loop of radius b is [7]

$$\vec{B} = \frac{\mu_o I b^2}{2r^3} \cos\theta\, \hat{u}_r + \frac{\mu_o I b^2}{4r^3} \sin\theta\, \hat{u}_\theta \tag{3}$$

where μ_o is the permeability of vacuum, I is the alternating current, and $\hat{u}_r$ and $\hat{u}_\theta$ are unit vectors in the directions of increasing r and θ, respectively. The assumption is made that $b << r$ and the sinusoidal time dependence has been suppressed. The magnitude of the vector $\vec{B}$ given by (eq 3) is B_o.

For our purposes, it is convenient to express $\vec{B}$ in terms of Cartesian coordinates. This is accomplished by using the following relations between spherical and Cartesian unit vectors and coordinates [8] in (eq 3):

$$\begin{aligned}
\hat{u}_r &= \hat{i} \sin\theta \cos\phi + \hat{j} \sin\theta \sin\phi + \hat{k} \cos\theta \\
\hat{u}_\theta &= \hat{i} \cos\theta \cos\phi + \hat{j} \cos\theta \sin\phi - \hat{k} \sin\theta \\
x &= \mathrm{r} \sin\theta \cos\phi \\
y &= \mathrm{r} \sin\theta \sin\phi \\
z &= \mathrm{r} \cos\theta
\end{aligned} \tag{4}$$

After some algebra, $\vec{B}$ can be expressed as

$$\vec{B} = \hat{i}\, \frac{3Cxz}{2r^5} + \hat{j}\, \frac{3Cyz}{2r^5} + \hat{k}\, \frac{C}{2r^3} \left(\frac{3z^2}{r^2} - 1 \right), \tag{5}$$

where $r = \sqrt{x^2 + y^2 + z^2}$ and C is the constant $\mu_o I b^2/2$.

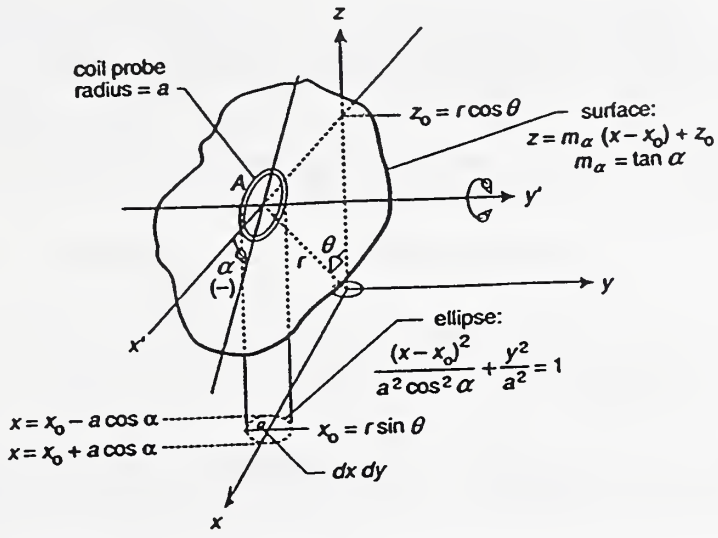

Figure 2. Circular coil probe shown as part of a surface described by the equation $z = m_\alpha\,(x - x_o) + z_o$. The rotation of the probe corresponds to changing the slope of the surface, m_α. The projection of the probe cross-sectional area onto the $x - y$ plane will be an ellipse for $\alpha \neq 0$. The range of α is -90° < α < 90°.

To obtain an expression for $B_{\rm av}$, we consider without loss of generality a probe with its center at $x = x_o$, $y = 0$, and $z = z_o$ as shown in Figure 2. We restrict the orientation of the probe so that its area is bisected by the $x - z$ plane and first consider rotations of the probe about an axis parallel to the y-axis, i.e., the y'-axis shown in Figure 2. For these conditions, the area of the coil probe, A, will be part of the surface given by the equation

$$z = m_\alpha(x - x_o) + z_o, \tag{6}$$

where α is the angle of rotation, $m_\alpha = \tan\alpha$, $x_o = r\sin\theta$, and $z_o = r\cos\theta$. The rotation of the probe corresponds to the rotation of this surface about the $y\prime$-axis, i.e., changing the slope of the surface (m_α) described by eq (6). It should be noted that the angle of rotation, α, shown in Figure 2 is in the negative direction.

The unit vector perpendicular to the probe surface, $\hat{n}$, is found by first taking the gradient [9] of the surface given by eq (6), $\nabla F(x,z)$, where $F(x,z) = z - m_\alpha(x - x_o) - z_o$ and normalizing it to unit value. This leads to

$$\hat{n} = (-m_\alpha\hat{i} + \hat{k})/\sqrt{m_\alpha^2 + 1}. \tag{7}$$

The element of area, dA, is [10]

$$dA = \sqrt{\left(\frac{\delta z}{\delta x}\right)^2 + \left(\frac{\delta z}{\delta y}\right)^2 + 1}\; dx\, dy = \sqrt{m_\alpha^2 + 1}\; dx\, dy. \tag{8}$$

where $dx\, dy$ is an element of area in the $x - y$ plane bounded by the projection of the probe cross section onto the $x - y$ plane (Figure 2).

Combining eqs (2), (5), (7), and (8), the expression for B_{av} becomes

$$B_{\text{av}} = \frac{C}{2\pi a^2} \int_x \int_y \left\{ \frac{-3xzm_\alpha}{r^5} + \frac{1}{r^3}\left(\frac{3z^2}{r^2} - 1\right)\right\} dx\, dy. \tag{9}$$

By substituting for z in eq (9) using eq (6), the integrand becomes a function of x and y. The integration is first carried out analytically [11] over the variable y with (from Figure 2)

$$-\sqrt{a^2 - ((x - x_o)/\cos\alpha)^2} \le y \le \sqrt{a^2 - ((x - x_o)/\cos\alpha)^2}.$$

The resulting expression for B_{av} is

$$\begin{aligned} B_{\text{av}} = -\frac{C}{\pi a^2} \int dx\, (m_\alpha\, x\, P + P^2) \Bigg\{ & \frac{\sqrt{a^2 - (\frac{x - x_o}{\cos\alpha})^2}}{(x^2 + Q^2)(x^2 + Q^2 + a^2 - (\frac{x - x_o}{\cos\alpha})^2)^{\frac{3}{2}}} \\ & + \frac{2\sqrt{a^2 - (\frac{x - x_o}{\cos\alpha})^2}}{(x^2 + Q^2)^2(x^2 + Q^2 + a^2 - (\frac{x - x_o}{\cos\alpha})^2)^{\frac{1}{2}}} \Bigg\} \\ & - \frac{C}{\pi a^2} \int dx \frac{\sqrt{a^2 - (\frac{x - x_o}{\cos\alpha})^2}}{(x^2 + Q^2)(x^2 + Q^2 + a^2 - (\frac{x - x_o}{\cos\alpha})^2)^{\frac{1}{2}}}, \end{aligned} \tag{10}$$

where $P = (z_o - m_\alpha\, x_o)$ and $Q^2 = (m_\alpha\, x + P)^2$.

The integration over x is then performed numerically using Simpson's Rule with the limits of integration given by (Figure 2)

$$x_o - a\cos\alpha \le x \le x_o + a\cos\alpha,$$

where α is restricted to -90° $< \alpha <$ 90°.

B_{av} is evaluated for fixed values of θ and r/a as α is varied until a maximum average flux density, B_{av1}, is found. B_{av1} is then compared with B_o. As noted earlier, the process is repeated for the same r/a but different values of θ until the largest

difference, ΔB_{max1}, is determined. Because we are seeking the maximum value of B_{av}, we do not consider further rotations of the probe because once B_{av1} is found, additional rotations are expected to lead to smaller values of B_{av}. This is most readily seen at θ equal to 0° and 90° for all values of r/a. B_{av1} occurs at $\alpha = 0°$, and rotating the probe further results in smaller values of B_{av}.

1.3.4 Three-Axis Probe

Although not shown in this report, expressions have been developed for the average magnetic flux density for each coil of a three-axis probe as the probe is rotated about axes which are parallel to the x-, y-, and z-axes. Afterwards, for fixed values of θ and r/a, the average magnetic field values from the three orthogonally oriented probes are combined according to eq (1) to obtain B_{av3} which is then compared with B_o. As before, the process is repeated for different values of θ until the maximum difference between B_{av3} and B_o, ΔB_{max3}, is found.

It is noted that combinations of rotations about the different axes will not be possible using the expressions that are developed. That is, it will not be possible to calculate B_{av3} following rotations about two or three axes. This represents a limitation on the results and prevents us from learning whether there are significant effects on the value of ΔB_{max3} due to multiple rotations. Nevertheless, the departures from B_o that are determined from rotations about each of the three axes will let us know what differences are possible as a function of r/a.

1.3.5 Results of Calculations

Using eq (10) and following the procedure described after eq (1), values of the maximum average magnetic field, B_{av1}, for fixed values of r/a and θ were calculated and compared with the corresponding value of B_o. Figure 3 shows the differences in percent between B_{av1} and B_o for $r/a = 3$ and for representative values of θ between 0° and 90° (because of symmetry arguments, one can infer the corresponding percentages for θ between 90° and 180°). The largest difference, ΔB_{max1}, is −14.6% and occurs when the single-axis probe is located along the axis of the magnetic dipole, i.e., the z-axis. The negative difference between B_{av1} and B_o decreases as θ increases and turns positive near $\theta = 90°$. This pattern also occurs for other values of r/a greater than 3. Figure 3 also shows the largest negative and positive differences in percent for r/a equal to 5, 8, 10, and 12. The largest negative differences must be considered part of the measurement uncertainty when the probe-dipole geometry is unknown, which will be the case for example when magnetic field measurements are performed near many appliances. A tabulation of ΔB_{max1}, as a function of r/a is given in Table 1.

The calculations are not carried out for large values of r/a because the accuracy requirements for magnetic field measurements near appliances and other electrical

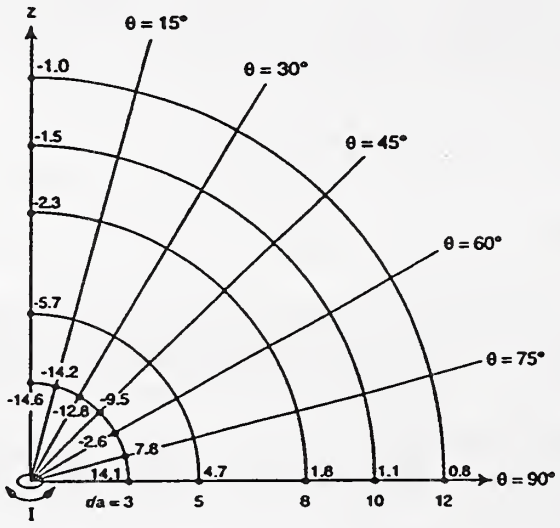

Figure 3. Differences between values of B_{av1} and B_{o}, in percent, for different locations of single-axis probe relative to magnetic dipole which is aligned along the z-axis. For a given value of r/a, where r/a is ≥ 3, the largest difference, ΔB_{max1}, is negative and occurs when the probe is located along the z-axis.

equipment either have not been set or are not great. For example, the uncertainty tentatively allowed during calibration of magnetic field meters used for measuring magnetic fields near visual display terminals is $\pm 5\%$ [12].

The differences between B_{av3} and B_{o} are considered in three steps, i.e., values of B_{av3} are calculated and compared with B_{o} following rotations about axes parallel to the x, y, and z axes. This is done for fixed values of r/a and representative values of θ between 0° and 90° (to take into account possible orientations of the dipole). The largest calculated differences were found to occur following rotations about axes parallel to the y-axis and the greatest differences (ΔB_{max3}) for fixed values of r/a ($0 \leq \theta \leq 90°$) are given in Table 1 [13].

1.3.6 Discussion of Results

Once it has been decided what constitutes an acceptable level of uncertainty during magnetic field measurements near electrical equipment, the information in Table 1 should be considered when taking into account the various sources of measurement uncertainty. For example, if maximum magnetic fields at a distance r from appliances are to be measured with a total uncertainty of less than $\pm 10\%$, magnetic field meters with probes having radii a such that $r/a \approx 3$ would immediately be considered unsuitable. Field meters with single-axis probes having radii such that $r/a = 5$ would be suitable if all other sources of uncertainty (e.g, calibration process, frequency

Table 1. Values of ΔB_{max1} (single-axis probe) and ΔB_{max3} (three-axis probe) as a function of normalized distance (r/a) from magnetic dipole.

r/a	$\Delta B_{\text{max1}}(\%)$	$\Delta B_{\text{max3}}(\%)$
3	-14.6	-19.6
4	-8.7	-10.8
5	-5.7	-6.9
6	-4.0	-4.8
7	-3.0	-3.5
8	-2.3	-2.7
9	-1.8	-2.1
10	-1.5	-1.7
11	-1.2	-1.4
12	-1.0	-1.2
13	-0.9	-1.0
14	-0.8	-0.9
15	-0.7	-0.8

response) amounted to about 8% or less, i.e., $\sqrt{5.7^2 + 8^2} = 9.8$, where 5.7 is taken from Table 1 for $r/a = 5$.

The measurement uncertainties associated with using three-axis probes are less clear because we have considered only separate rotations about three axes to obtain the values of ΔB_{max3}. The percentage differences in Table 1 indicate what uncertainties can occur, but they may not be the largest uncertainties due to the averaging effects of the probe. However, until calculations can be devised which consider more complex rotations of three-axis probes, the ΔB_{max3} values in Table 1 can serve as a rough guide when deciding what are acceptable probe dimensions.

2 GASEOUS DIELECTRICS RESEARCH

Task 02
Richard J. Van Brunt, James K. Olthoff, Kenneth L. Stricklett
David Wheeler, and Eric W. Cernyar
Electricity Division
National Institute of Standards and Technology

John T. Herron
Chemical Kinetics Division
National Institute of Standards and Technology

J. H. Moore and J. A Tossell
Department of Chemistry and Biochemistry
University of Maryland
College Park, MD 20742

2.1 Introduction

The objectives of this project are the development of measurement capabilities and the providing of fundamental data as part of the Department of Energy's basic research concerned with the development and evaluation of advanced compressed-gas insulation technology.

To reduce space requirements and improve the efficiency of high-voltage transmission systems, the electric power industry has turned toward more extensive use of compressed-gas-insulation. To design meaningful tests of system performance and establish specifications for the quality of materials used in such systems, more information is needed about the fundamental physical and chemical processes which lead to insulation deterioration and electrical breakdown. The research includes applications of gas chromatography-mass spectrometry to characterize corona discharge by-products; and the acquisition of fundamental data, such as reaction-rate coefficients, corona-inception voltages, production rates of corona by-products, the effects of contaminants on discharge initiation, and the rates of discharge-induced decomposition of the gas.

During the past year, the NIST gaseous dielectrics research activities have been incorporated into a Cooperative Research and Development Agreement (CRADA) that has been established to study the production and mitigation of S_2F_{10} (disulfur decafluoride) in compressed SF_6–Insulated Power Systems. Support for the CRADA research has been received from the U.S. Department of Energy (Office

of Energy Management), the Electric Power Research Institute, The Bonneville Power Administration, the Tennessee Valley Authority, the Empire State Electric Energy Corporation, the Canadian Electrical Association, and Ontario Hydro. The research participants in the CRADA are: NIST, the Oak Ridge National Laboratory (operated by Martin Marietta Energy Systems, Inc.) and the Ontario Hydro Research Laboratory. The current research activities of the CRADA members are discussed in a recent publication [14].

The particular concern about S_2F_{10} is due to its highly toxic nature and the fact that it is known to be formed when SF_6 decomposes in electrical discharges. The Ceiling Limit Value for human exposure to S_2F_{10} is 10 parts per billion (ppb) or equivalently 1 part in 10^8. The purposes of the CRADA research are: 1) to develop methods for detecting S_2F_{10} in SF_6 down to the 10 ppb level; 2) to determine the conditions under which S_2F_{10} will most likely form in power systems, e.g., during corona or spark discharges; 3) to determine the stability, toxicity, and thermal/chemical properties of S_2F_{10}; and 4) to investigate methods for removing S_2F_{10} from decomposed SF_6. The motivation for this work is to ensure continued safe operation and maintenance of SF_6–insulated equipment by providing information needed to access potential hazards and by recommending procedures for mitigation of hazards.

Methods recently developed to detect S_2F_{10} in SF_6 at NIST and the other participating CRADA laboratories have been described [15–17]. A gas chromatograph-mass spectrometer method has been developed at NIST with a sensitivity of 2 ppb [15] and is now being used to measure S_2F_{10} production from SF_6 corona discharges [18] and in SF_6 exposed to x-rays. It is also being used in collaboration with the Ontario Hydro Laboratory in conducting a survey of SF_6–power equipment that is now or has been in service.

This section of the report highlights progress of research in two areas, namely 1) measurement of dissociative electron attachment cross sections and negative ion production in S_2F_{10}, S_2OF_{10}, and $S_2O_2F_{10}$, and 2) Monte-Carlo simulation of ac-generated partial-discharge pulses that can occur in SF_6–insulated power systems and can be sources of gas decomposition. The first of these activities is an extension of an investigation that covered other by-products of SF_6 decomposition such as SO_2, SOF_2, SOF_4, SO_2F_2, and SF_4. The results of this earlier work have been published in Plasma Chemistry Plasma Processing [19] and the results presented here have been published in the Journal of Chemical Physics [20]. Preliminary results from the Monte-Carlo simulation have been reported in a recent conference paper [21].

2.2 Dissociative Electron Attachment to S_2F_{10}, S_2OF_{10}, and $S_2O_2F_{10}$

2.2.1 Introduction

The work described in this section was carried out in a collaboration with scientists at the University of Maryland and at the Oak Ridge National Laboratory, and is part of our on going efforts to develop more sensitive techniques for detecting S_2F_{10} and related compounds and to better understand the chemical processes that can affect their formation in SF_6–insulated systems.

The compounds disulfur decafluoride (S_2F_{10}), bis(pentafluorosulfur) oxide (S_2OF_{10}), and bis(pentafluorosulfur) peroxide ($S_2O_2F_{10}$) are chemically related to SF_6, formed from the reaction products of sulfur and fluorine in the presence of oxygen, and known to be thermally stable in the gaseous state at room temperature (20°C) [22–29]. All three compounds can be formed by electrical discharges in SF_6 and SF_6/O_2 gas mixtures under a wide range of conditions [18, 30–32]. In the case of S_2F_{10}, which is known to be highly toxic [33], there is a need to develop methods for detecting trace levels of this species in the presence of SF_6. One of the proposed methods of analysis for S_2F_{10} employs an electron capture detector coupled to a gas chromatograph [16, 34]. Since the transport times of S_2OF_{10} and $S_2O_2F_{10}$ through a chromatographic column can be comparable to that of S_2F_{10}, it is possible that these compounds will interfere with the detection of S_2F_{10}. Information about negative-ion formation processes for these molecules is needed to assess the importance of such interference.

Little is known about the processes of negative-ion formation in S_2F_{10}, S_2OF_{10} and $S_2O_2F_{10}$ at electron impact energies less than 10 eV. The molecular structures are known [35–38] and processes forming positive ions have been investigated [24, 39, 40]. In its ground electronic state, S_2F_{10} has a linear structure (F_5S–SF_5) with a relatively weak S–S bond. The molecules S_2OF_{10} and $S_2O_2F_{10}$ have nonlinear structures with weak O–S and O–O bonds, respectively.

The present work was undertaken to determine the absolute cross sections for dissociative electron attachment to S_2F_{10}, S_2OF_{10}, and $S_2O_2F_{10}$, and to identify the negative-ion fragments that are formed in the process. Dissociative attachment can be viewed as a resonant electron scattering process that results in formation of a temporary, anti-bonding negative-ion state that decays into a negative ion and one or more neutral fragments. The process allows formation of energetically stable negative ions as well as neutral fragments that may be in excited states. The approach used in the present work is essentially identical to that used in recent investigations [19, 41] of the compounds SO_2, SOF_2, SOF_4, SO_2F_2, and SF_4.

2.2.2 Measurement Methods

The absolute cross sections for dissociative electron capture were measured with an electron transmission spectrometer [19, 42]. The instrument consists of a thermionic electron source followed by a trochoidal monochromator, an accelerating lens, gas cell, and retarding lens that permits only unscattered electrons to be transmitted to a collector at which the transmitted current is measured. The instrument is immersed in a uniform magnetic field of about 7 mT (70 gauss). Cross sections for dissociative attachment processes are determined by measuring the product negative-ion current at the walls of the scattering cell. More details of the apparatus and experimental procedure are given elsewhere [45].

For the electron transmission studies, the electron-energy resolution was approximately 50 meV. The energy scale was determined by mixing nitrogen with the sample gas and observing the vibrational structure in the transmitted electron current due to electron scattering associated with the well known $^2\Pi_g$ shape resonance of N_2 centered around 2.3 eV [44]. The uncertainty in the calibration of the energy scale is estimated to be less than 50 meV. Pressures in the collision cell were maintained between 0.02 and 0.05 Pa (0.15 to 0.38 mTorr) for all data presented here, and the temperature within the scattering region was maintained at room temperature.

The largest uncertainties in the measurement are associated with the measurement of the target gas pressure and with our estimate of the length of electron trajectories through the target cell. The accuracy of the pressure measurement, accessed by intercomparison of the capacitance manometer with two absolute pressure gauges, is estimated to be $\pm 11\%$, introducing a corresponding uncertainty into the reported cross section. The presence of the magnetic field imparts a helical motion to the electrons and hence introduces an uncertainty in the path length through the target. This effect increases with decreasing electron energy. The reported cross sections take the path length equal to the physical length of the cell, thus overestimating the cross section to the extent to which the helical motion increases the length over which the electrons can interact with target molecules. This effect has been discussed quantitatively in earlier publications [43, 45]. If one takes the most conservative approach, assuming that all of the thermal motion of electrons leaving the source is directed radially, the reported cross section would be too large by a factor of 1.1 for 1.0 eV electrons passing through the target, a factor of 1.2 at 0.5 eV, 1.4 at 0.2 eV, and 1.9 at 0.1 eV. It should be emphasized that these are maximum estimated errors. Scattering cross sections for nitrogen obtained with this instrument compared to measurements made by different methods [43] suggest that the problem associated with the uncertainty in the path length is much less severe than implied by this worst case estimate.

Fragment-ion identifications were made from independent measurements using a linear time-of-flight (TOF) mass spectrometer as previously described [41, 46, 47].

This system uses a pulsed electron beam from a thermionic emission source to produce negative ions, which are then accelerated into a field-free drift tube. The electron energy spread in this experiment is estimated to be 0.5 eV from observation of SF_6^- ions produced by resonant electron capture in pure SF_6 at threshold electron energies.

The relative intensities of the different ions were determined from TOF measurements made at different electron-impact energies. Negative ions which decay by dissociation or electron detachment in the flight tube are detected since the neutral fragments possess sufficient kinetic energy to trigger the detector. The contribution of short-lived ions to the detected signal is assessed with the use of a pair of electrostatic deflection plates at the down stream end of the flight tube. Only neutral fragments are detected when the deflection field is applied. Ions with lifetimes longer than the drift-tube flight time can reach the detector only when the deflection field is off. For the measurements discussed here, the TOF system was operated at gas pressures between 10^{-3} to 1.5×10^{-2} Pa.

The S_2F_{10}, S_2OF_{10}, and $S_2O_2F_{10}$ samples had an estimated purity of greater than 99% at the time of preparation. Sample purities were confirmed prior to use with a gas chromatograph-mass spectrometer [15].

2.2.3 Results

Absolute dissociative electron-attachment cross sections for S_2OF_{10} and $S_2O_2F_{10}$ are shown in Figure 4, and for comparison, the electron-attachment cross section for SF_6 recently measured with the same instrument is included. Comparison of this electron-capture cross section for SF_6 has been shown in Ref. 24 to be in agreement with other measurements and demonstrates the suitability of the experimental technique for these types of measurements. In the energy range shown, the electron attachment process in SF_6 is known [48] to yield primarily SF_5^- for electron energies above 0.2 eV and SF_6^- at lower energies. Cross sections for both S_2OF_{10} and $S_2O_2F_{10}$ are extraordinarily large at low energies, exceeding the maximum for the SF_6 cross section by about two orders of magnitude.

Figures 5 and 6 show, respectively, the negative-ion yields for S_2OF_{10} and $S_2O_2F_{10}$, observed with the TOF mass spectrometer. The species S_2OF_{10} yields primarily SOF_5^-. The yields of other ions are at least two orders of magnitude lower than that for SOF_5^-. In the case of $S_2O_2F_{10}$, the threshold attachment process results in the production of either SOF_5^- or SF_5^- with similar intensity. There is also evidence for formation of SOF_3^- and F^- from this resonance with much lower probability. However, there are other possible sources of SOF_3^- in the TOF instrument as will be discussed below.

The absolute dissociative-attachment cross section data for S_2F_{10}, shown in Figure 7, exhibit a peak near zero energy, similar to but smaller than the other compounds, as

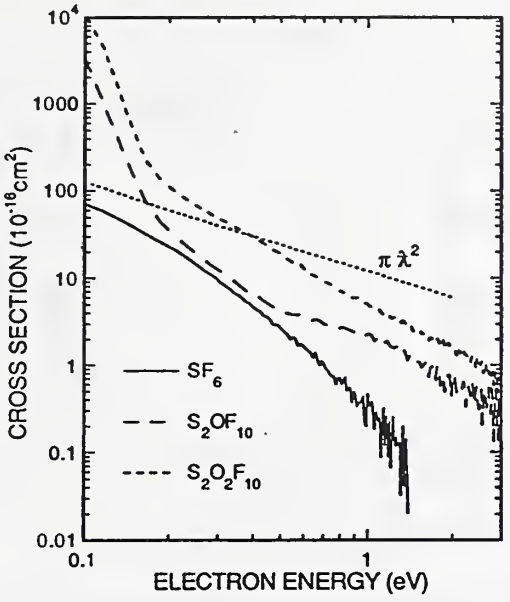

Figure 4. Electron-energy dependence of the absolute cross sections for dissociative electron attachment to S_2OF_{10} (dashed line) and $S_2O_2F_{10}$ (dotted line) in comparison with the previously measured [41] electron attachment cross section for SF_6 (solid line) and calculated maximum s-wave capture limit ($\pi\lambda^2$).

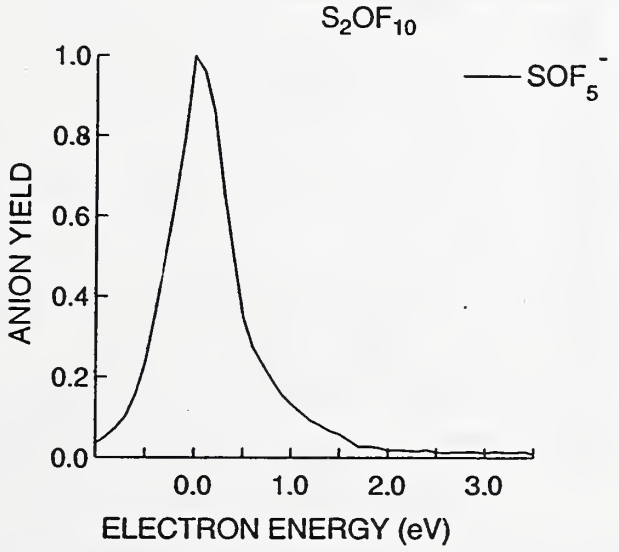

Figure 5. Electron-energy dependence of the anion yield from S_2OF_{10} using the TOF mass spectrometer.

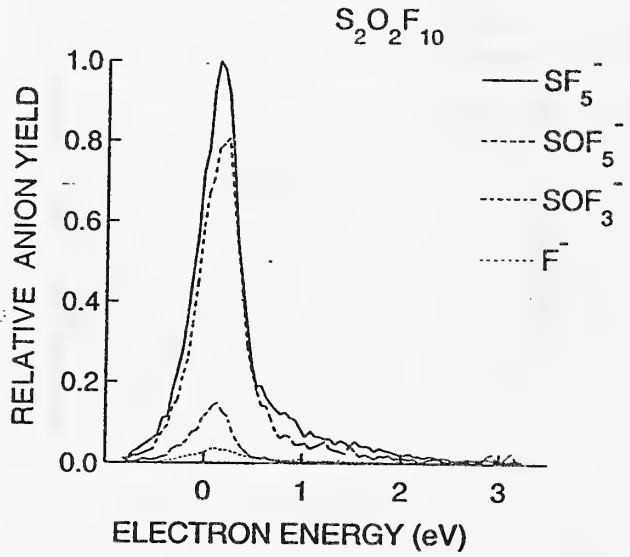

Figure 6. Electron-energy dependence of the anion yield from $S_2O_2F_{10}$ using the TOF mass spectrometer.

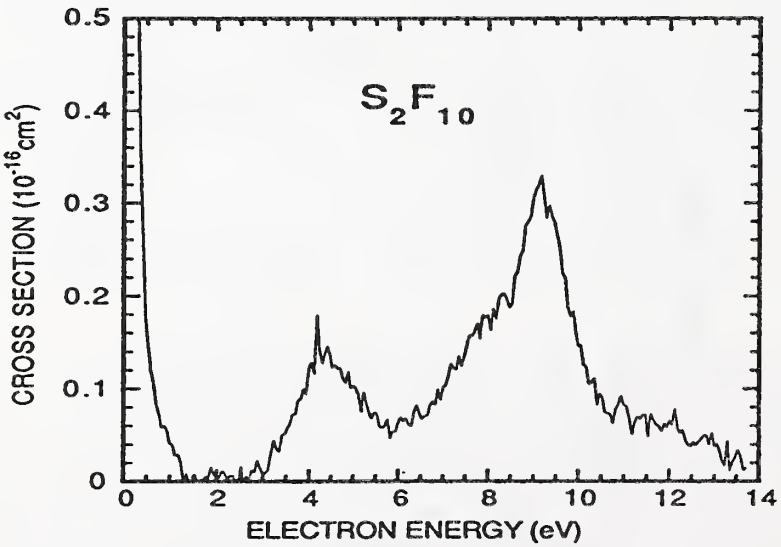

Figure 7. Electron-energy dependence of the absolute cross section for dissociative electron attachment to S_2F_{10}.

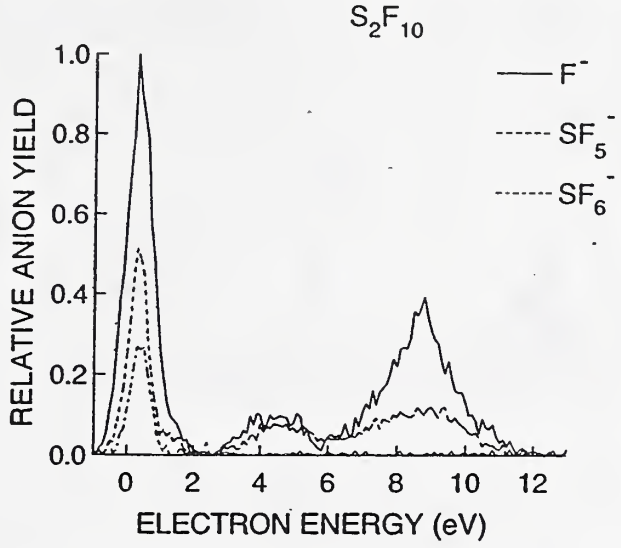

Figure 8. Electron-energy dependence of the anion yield from S_2F_{10} using the TOF mass spectrometer.

well as two smaller features at about 4.5 and 9.5 eV. The corresponding data from the TOF mass spectrometer experiment are shown in Figure 8. The predominant negative ions formed in all three resonance processes are F^- and SF_5^-. There is also evidence for the production, with low probability, of SF_6^- and SF_4^- in the threshold attachment process.

It should be noted that the raw data for the absolute cross section are complicated by a background current, which becomes significant at electron energies above 6 eV. This current is due to electrons that experience multiple scattering within the collision region, thus permitting them to cross magnetic field lines and reach the wall of the gas cell and contribute to the measured current. The TOF data are free of this effect, and were used to estimate a correction for the data shown in Figure 7.

When S_2F_{10} was introduced into the TOF mass spectrometer, a peak appeared at mass 105 u corresponding to SOF_3^- (see Figure 9). It is known that S_2F_{10} can readily react on hot surfaces with adsorbed H_2O to form oxyfluorides [15, 25]. Thus the SOF_3^- most likely is formed by reactions of S_2F_{10} on the surfaces near the filament. Moreover, there is evidence [30] that SF_5 radicals from dissociation of S_2F_{10} react with OH to form SOF_4 at low pressures. Dissociation of gas-phase water near the hot filament in the TOF apparatus may produce OH; thus SOF_4 may be formed in the region near the filament. Previous work [41] has shown that dissociative attachment to SOF_4 leads predominantly to SOF_3^- with relatively large probability near zero energy. The SF_4 could also form SOF_5^-, (which was also observed in the S_2F_{10} TOF mass spectrum), through fast F^- transfer reactions [49].

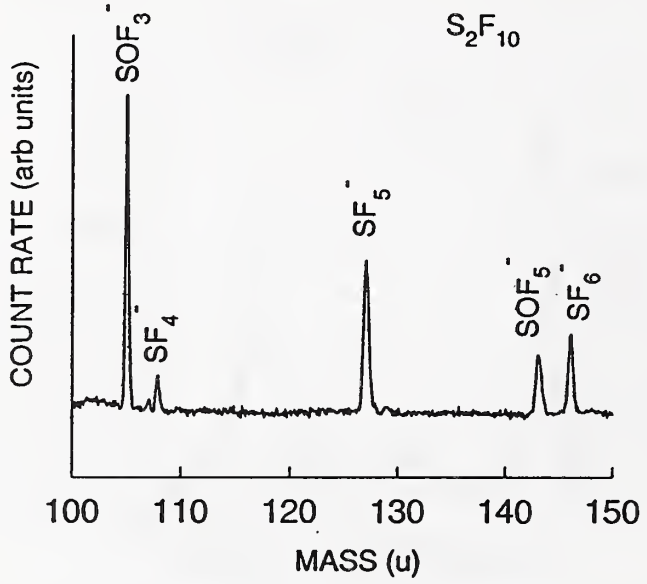

Figure 9. Typical negative-ion mass spectrum from S_2F_{10}.

The presence of SOF_4 in the mass spectrometer would not affect our assignment of ions to S_2F_{10} as indicated in Figure 8; however, it could have an effect on the results for $S_2O_2F_{10}$ shown in Figure 7. Experiments in our laboratories and elsewhere [24] have shown that $S_2O_2F_{10}$ is thermally unstable on hot surfaces, and can decompose into reactive species like SF_5 that form SOF_4. For this reason, the assignment of the ion SOF_3^- to $S_2O_2F_{10}$ must be considered tentative.

2.2.4 Discussion

No parent negative ions ($S_2F_{10}^-$, $S_2OF_{10}^-$, or $S_2O_2F_{10}^-$) were detected in the TOF experiment. This implies that, even at thermal energies ($< 0.1\,eV$), electron attachment to S_2F_{10}, S_2OF_{10}, and $S_2O_2F_{10}$ results in dissociation. Although the calculations discussed in the next section indicate that $S_2F_{10}^-$ and $S_2O_2F_{10}^-$ are stable, the formation of these ions requires collisional stabilization that is improbable at the low pressures in the TOF apparatus.

It is surprising that both S_2OF_{10} and $S_2O_2F_{10}$ have such large attachment cross sections, among the largest observed for any molecule. As can be seen in Figure 4, the cross sections for electron capture to $S_2O_2F_{10}$ and S_2OF_{10} exceed the theoretical limit (by significantly more that the estimated measurement uncertainties) for s-wave capture imposed by the Wigner threshold condition [50] for scattering from a central potential as considered by others [51] in the interpretation of data on electron attachment. However, contributions from other partial waves can be significant for electron interactions above thermal energies [51]. Moreover, there is reason to question the applicability of partial-wave analysis and therefore the s-

wave limit to electron scattering from the large, nonspherically symmetric molecules considered here for which the interaction potentials are multicentered. Additionally, the consistency of the results presented here for $S_2O_2F_{10}$ and S_2OF_{10} with the s-wave limit near zero energy is impossible to assess since the present data do not extend below 0.1 eV. The behavior of electron capture cross sections for very low energy electrons (< 100 meV) would be better investigated using the experimental techniques of Chutjian and coworkers [51] or Klar and coworkers [52].

The fact that SOF_5^- is the predominant negative ion formed from dissociative electron attachment to S_2OF_{10} is consistent with the assumption of a relatively weak sulfur-oxygen bond in the intermediate parent negative-ion state. The formation of either SF_5^- or SOF_5^- from $S_2O_2F_{10}$ with nearly equal probability implies a rupture of one of the O–O or S–O bonds.

Similar to S_2OF_{10} and $S_2O_2F_{10}$, S_2F_{10} exhibits a large (greater than $10^{-16}\,cm^2$) cross section for dissociation near zero energy. In addition, two attachment resonances occur at higher energies (4.5 and 9.5 eV). Both result in the formation of F^- and SF_5^-. For the 4.5-eV process, both fragment ions appear with nearly equal probability, whereas F^- appears to predominate at the 9.5-eV resonance. The formation of SF_5^- is expected if the dissociation occurs along the weak sulfur-sulfur bond. It is speculated that F^- formation at the high-energy resonances results predominantly from an indirect process involving decay of the SF_5^- anion formed in its lowest antibonding state. The recent calculations of Ziegler and Gutsev [53] indicate that the dissociation channel of lowest energy for the SF_5^- anion leads to F^- formation. The dissociation energy for SF_5^- is estimated to be 2.9 eV. Based on estimates of the heats of formation and on the uncertainties of these estimates for S_2F_{10} and S_2F_9, [30] direct formation of F^- can occur at 0.5 ± 0.46 eV electron energy, indicating that a direct dissociative attachment process for F^- formation at thermal energy is possible. Similarly, using 2.7 ± 0.2 eV for the electron affinity [54] of SF_5, SF_5^- formation by direct dissociative attachment to S_2F_{10} is possible at thermal electron energies, from an estimated heat of reaction of -0.75 ± 0.48 eV. Thus, the F^- and SF_5^- ions observed at zero electron energy can be attributed to direct dissociative electron attachment to S_2F_{10}.

The suggestion of thermal decomposition of S_2F_{10} in the TOF apparatus raises the possibility that some of the observed SF_6^- may not come from electron attachment to S_2F_{10} since thermal decomposition of this substance is known to produce SF_6 [15, 25–27]. On the other hand, it is also known that SF_6^- produced by low-energy electron attachment to SF_6 has a lifetime for autodetachment of a few microseconds to milliseconds depending upon the state in which it is formed [55]. Tests using the deflection plates in the mass spectrometer flight tube gave no evidence for the presence of short lived SF_6^-, implying that the observed signal originated from a dissociative-attachment process. Thus, the possibility that SF_6^- is indeed formed directly from electron attachment to S_2F_{10} cannot be ruled out. The process may be the consequence of a structural rearrangement [36].

2.2.5 Calculations

To help in understanding the electron attachment behavior of S_2F_{10}, S_2OF_{10}, and $S_2O_2F_{10}$, we have carried out *ab initio* Self-Consistent-Field (SCF) calculations on the neutral molecules and their anions, much like those performed earlier [56] on simpler molecules such as SF_4. For comparison, we have also included SF_6 in our calculations, as it provides a test of the accuracy of the calculational method. Unpolarized split-valence bases at geometries optimized using polarized split-valence bases were employed for SF_6, S_2F_{10} (D_{4d}), and S_2OF_{10} (C_{2v}). The $S_2O_2F_{10}$ is too large and asymmetric to use polarized split-valence bases for geometry optimization. Its geometry was optimized only at the semiempirical PM3 level [57]. Calculated geometries of SF_6 and S_2F_{10} have been reported previously [56]. All calculations were performed with the program GAMESS [58]. The bond lengths (R) for S_2OF_{10} at the 3-21G SCF level were calculated to be R(S–O)=0.1618 nm and R(S–F)=0.1537–0.1542 nm, and the angle formed by the S–O–S bonds was calculated to be 155°, in reasonable agreement with the experimental values [37] of 0.1586 nm, 0.1558–0.1572 nm and 142.5°, respectively. For $S_2O_2F_{10}$ the PM3 optimized geometry has R(O–O)=0.1479 nm, R(S–O)=0.178 nm, R(S–F)=0.1551–0.1561 nm, and the S–O–O angle equal to 136° compared to experimental values [38] of 0.143 nm, 0.166 nm, about 0.156 nm, and 111°, respectively.

Calculated electron attachment energies of SF_6, S_2F_{10}, S_2OF_{10}, and $S_2O_2F_{10}$ are compared with the energies of experimentally observed resonances. For the present discussion, the attachment energy (AE) is defined as the internal energy change when an electron is captured by a neutral gaseous molecule. The AE is therefore positive if the resulting anion is less stable than the neutral molecule. Calculated vertical attachment energies assume no change in the geometry of the molecule during the electron capture process, while adiabatic attachment energies allow for changes in the anion geometry, leading to a new minimum energy geometry.

Vertical electron attachment energies for the four molecules as derived from the virtual orbital eigenvalues, ε_i, (i.e., within Koopmans' approximation) and as differences in total SCF energies of the anion and the neutral (ΔE_{SCF}) are given in Table 2. The ΔE_{SCF} and the ε_i give only approximate values for the attachment energy. For those cases in which ΔE_{SCF} is negative at the geometry of the neutral, corresponding to a bound state anion, the ΔE_{SCF} method is valid but ignores correlation differences between the neutral and the anion. We have also employed a small basis with none of the diffuse functions needed to accurately describe the anion electron density. For cases in which ΔE_{SCF} is positive, the anion is unbound, technically a scattering resonance, so our bound state approach is not formally correct. Our results will be unstable toward the addition of diffuse and/or continuum basis functions. This difficulty can be removed in simpler cases using stabilization methods [59]. Even without stabilization, calculations using split-valence bases often give results

in reasonable agreement with experiment using the ΔE_{SCF} approach as we have demonstrated for some smaller sulfur oxyfluorides [56].

The calculated ΔE_{SCF} falls approximately 1 eV below the ε_i for the ground-state anion of each compound. It is expected that this "shift" is qualitatively applicable to the higher-energy states, and the calculations of ε_i may thus be used to estimate the energies of higher-energy scattering resonances [56]. For SF_6, the calculated AE for the a_{1g} orbital (or scattering resonance) at the ΔE_{SCF} level is 2.2 eV, in reasonable agreement with the experimental resonance position of 2.5 eV [60]. The eigenvalue of the t_{1u} orbital less 1 eV is 7.4 eV, compared to an experimental value of 7.0 eV [60]. Differences between calculations and experimental values are expected to increase for molecules of lower symmetry. Estimating AEs of S_2F_{10} as ε_i minus 1 eV would suggest resonances at about 5.5, 6.3, and 7.8 eV. These energies are near the values of the two higher-energy features in Figures 7 and 8. It is difficult to assign particular orbitals to these features since the calculations provide no estimates of the intensity of a resonance. The a_2 state of $S_2F_{10}^-$ and the a state of $S_2O_2F_{10}^-$ are calculated to be stable at the ΔE_{SCF} level at the neutral geometries; however, since no evidence of parent ion formation for S_2F_{10} and $S_2O_2F_{10}$ was observed in the data, it can be assumed that the lifetimes of these metastable ions are less than 1 μs.

Adiabatic AE values will be more negative than vertical AEs. For SF_6, we calculate an adiabatic AE of −1.4 eV (i.e., an electron affinity of +1.4 eV) while the experimental value is about −1.0 eV [61]. For S_2F_{10} and S_2OF_{10}, the calculated adiabatic AEs are −5.2 and −2.6 eV, respectively. These values are given in Table 3.

The bonding character of the virtual molecular orbitals to which electrons are added in these molecules can provide some understanding of the anions produced by dissociative attachment. In general, if a virtual orbital is antibonding between two atoms we would expect the bond between them to have a higher probability of breaking. The $^2A_{1g}$ state of SF_6^-, formed by populating the a_{1g} lowest unoccupied molecular orbital (LUMO), shows an elongated S–F bond as in previous studies [62], and is consistent with formation of F^- and SF_5^-. For S_2F_{10}, the a_2 LUMO is S-Sσ^* and S-Fσ^* in character, consistent with rupture of the S–S or S–F bond to give SF_5^- or F^- fragments. At the 3-21G SCF level in D_{4d} symmetry, the S–S bond distance increases by 0.042 nm and the S–F bond distances increases by 0.002–0.005 nm when an electron is added to S_2F_{10}. Similarly, for S_2OF_{10} at the 3-21G level, electron addition gives an increase in S–O distance of 0.013 nm and an increase in S–F distances of 0.09 to 0.013 nm.

2.2.6 Conclusions

The dissociative attachment cross sections measured for S_2OF_{10} and $S_2O_2F_{10}$ are among the largest reported for any gas-phase molecule. These exceptionally large cross sections make S_2OF_{10} and $S_2O_2F_{10}$ of particular interest in investigations of low-

energy electron-attachment processes of gaseous dielectrics. Because of the magnitude of these cross sections, it can be concluded that the presence of S_2OF_{10} and $S_2O_2F_{10}$ may cause significant interference in the detection of S_2F_{10} by gas chromatographic techniques utilizing electron capture detectors.

The apparent production of stable SF_6^- by dissociative electron attachment to S_2F_{10} is of significance. Experimental investigations of SF_6^- have long been hampered by the difficulties of producing the ions with known internal energy. The long lifetimes of the SF_6^- ions observed here indicate that this dissociative attachment process may represent a possible source of SF_6^- in a well-defined state. Unambiguous determination of the source of SF_6^- from S_2F_{10} would require modifications to the TOF mass spectrometer to remove the hot electron source from the collision region. Assembly of this type of electron source/collision cell for a different mass spectrometer system is currently under way.

Table 2. Vertical electron attachment energies for SF_6, S_2F_{10}, S_2OF_{10}, and $S_2O_2F_{10}$ obtained from virtual orbital eigenvalues (ε_i) and anion-neutral total energy differences (ΔE_{SCF}) using 3-21G bases at 3-21G† SCF optimized geometries.

Molecule	Label and nature of virtual orbital	ε_i (eV)	ΔE_{SCF} (eV)
SF_6	a_{1g}, S-Fσ^*	3.2	2.2
	t_{1u}, S-Fσ^*	8.4	-
S_2F_{10}	a_2, S-Sσ^*, S-Fσ^*	0.2	–0.8
	e_1, S-Sπ^*, S-Fσ^*	6.5	-
	a_2, S-Sσ^*, S-Fσ^*	7.3	-
	e_3, S-Sπ^*, S-Fσ^*	8.8	-
S_2OF_{10}	a_1, S-O-Sσ^*	1.9	0.9
$S_2O_2F_{10}$	a, O-Oσ^*, S-Sσ^*	0.5	–1.0

†geometry optimized at the semiempirical PM3 level, anion calculation at restricted open shell Hartree-Fock level.

Table 3. Comparison of calculated vertical and adiabatic electron attachment energies for SF_6, S_2F_{10}, and S_2OF_{10}. The experimental values are shown in parentheses for SF_6. Adiabatic AE's are obtained as the total energy of the relaxed geometry anion minus the energy of the geometry optimized neutral.

Molecule	Orbital	ΔE_{SCF} (eV)	Adiabatic AE (eV)
SF_6	a_{1g}	2.2 (2.6)	–1.4 (–1.0)
S_2F_{10}	a_2	–0.8	–5.2
S_2OF_{10}	a_1	0.9	–2.6

2.3 Monte-Carlo Simulation of Partial Discharge

2.3.1 Introduction

Partial discharge (PD) generally occurs at defect sites, such as cracks, cavities, and asperities, in high-voltage electrical insulation, and is the consequence of local enhancements of the electric-field strength at these sites. The occurrence of PD in solid insulation is usually considered to be undesirable because of the material damage that it produces at the discharge site that can eventually result in a complete electrical breakdown. In gaseous dielectrics such as SF_6, PD can be a major source of toxic and corrosive by-products such as S_2F_{10}, S_2OF_{10} and $S_2O_2F_{10}$ considered in the previous section. In order to be able to quantify the rate of production of gaseous by-products from PD in SF_6, more must be understood about the nature of this phenomenon, particularly the factors that control its voltage and current characteristics. The phenomenon under consideration here is a pulsating discharge that can usually be represented by a random point process [63–65]. It has been shown from recent experimental investigations [63–65] that the statistical properties of pulsating partial-discharge (PD) phenomena are significantly influenced by effects of pulse-to-pulse and/or phase-to-phase memory propagation. The sources of the memory are dissipating residuals from the discharge pulses such as ion space charge, surface charge, and molecular species in excited states.

Previous "deterministic" models for ac-generated PD [66], although useful in providing insight into the physical basis for discharge patterns, do not account for the observed statistical behavior. Recent attempts [67] to develop Monte-Carlo simulations of PD that produce the required statistical variability have not been tested to determine that they account for known memory effects. In the present work, a Monte-Carlo simulation of ac-generated PD pulses is described which can properly account for effects of phase-to-phase memory propagation. The results of the simulation have been tested by determination of various unconditional and conditional pulse amplitude, phase-of-occurrence, and integrated charge distributions. The stochastic behavior of the simulated pulses is shown to be similar to that found experimentally for ac-generated PD in point-to-dielectric discharge gaps [64, 68].

2.3.2 Physical Model

The theoretical model used to make the simulation reported here is applicable to discharge gaps in which at least one of the surfaces is composed of a dielectric material, e.g., a metal point-dielectric plane gap, or a dielectric-dielectric gap such as might correspond to a void in a solid insulator. The basic assumptions of the model are:

1. The PD pulses are initiated by electrons released from surfaces by quantum mechanical tunneling, e.g., a Fowler-Nordheim field emission [69].

2. The pulses have a quasi-normal (Gaussian) distribution of amplitudes about a mean sufficient to cause a drop in the local electric-field strength to quench the discharge and prevent immediate reinitiation of the next pulse, and small enough to prevent a complete field reversal at the discharge site.

3. The charge deposited on the dielectric surface by a PD event and the corresponding local field reduction are directly proportional to the PD amplitude.

4. The dielectric surface charge is quasi-permanent, i.e, it decays at a rate much slower than the frequency of the applied voltage.

5. The applied voltage is sinusoidal, i.e.,

$$V(t) = V_o \sin \omega t \tag{11}$$

where V_o is the amplitude and ω the frequency; and the local surface field at the discharge site has a magnitude proportional to $|V(t)|$, i.e, $|E(t)| \propto |V(t)|$.

According to the first assumption above, the rate of electron release from a surface at any time t is given by

$$r_e^{\pm}(t) = C_1^{\pm} |E(t)|^2 \exp(-C_2^{\pm}/|E(t)|), \tag{12}$$

where the positive and negative superscripts refer to the two possible directions of the field and $C_1^{\pm}, C_2^{\pm}$ are constants which are in general different for + and − if there are gap asymmetries or differing dielectric and metal electrodes. These constants can be expressed in terms of effective work functions Φ_+ and Φ_- [69, 70] i.e.,

$$C_1^{\pm} = (1.54 \times 10^{-6}/\Phi_{\pm}) \times 10^{(4.52\Phi_{\pm}^{-0.5})}, \tag{13}$$

$$C_2^{\pm} = 6.83 \times 10^9 \Phi_{\pm}^{1.5}, \tag{14}$$

where $\Phi_{\pm}$ is in units of eV if $E(t)$ is in units of V/cm.

The probability that an electron will be released at an arbitrary time between t and $t + \Delta t$ is given by

$$P_i^{\pm}(t)\Delta t = 1 - \exp(-r_e^{\pm}(t)\,\Delta t). \tag{15}$$

In the computer simulation, the period of the applied voltage, $T = (2\pi/\omega)$, is segmented into equal increments, Δt, where $T \gg \Delta t$, and $r_e^{\pm}(t)$ is evaluated for the field value at time $t = n\Delta t + \Delta t/2$, where n is an integer increment number such that $T \geq n\Delta t \geq 0$. An electron is ejected at time t if $R \leq P_i^{\pm}(t)\Delta t$, where R is a uniformly distributed random number generated by the computer in the interval (0, 1).

Using assumption (2), the probability that a PD pulse formed at a time t will have an amplitude in a range $q^{\pm}$ to $q^{\pm} + dq^{\pm}$ is determined from a Gaussian random number generator so that it is given by

$$P_a^{\pm}(q^{\pm}, t)\, dq^{\pm} = [2\pi\sigma^{\pm}(t)]^{-\frac{1}{2}} \exp\left[\frac{1}{2}\left(\frac{q^{\pm} - \mu^{\pm}(t)}{\sigma^{\pm}(t)}\right)^2\right] dq^{\pm}, \tag{16}$$

where, for cases considered here, $\mu^{\pm}$ and $\sigma^{\pm}$ are given by

$$\mu^{+}(t) = (E(t) - E_I^{+}) + (0.2 + 0.1R)E_I^{+} \tag{17}$$

$$\sigma^{+} = (0.35 + 0.1R)E_I^{+} \tag{18}$$

$$\mu^{-}(t) = (E(t) + E_I^{-}) - (0.1 + 0.1R)E_I^{-} \tag{19}$$

$$\sigma^{-} = -(0.6 + 0.1R)E_I^{-}. \tag{20}$$

Here $E_I^{\pm}$ are adjustable constants that determine the mean local field reduction due to a discharge pulse and satisfy the condition $|E_c| \geq |E_I^{\pm}| > 0$, where E_c is a critical field required for growth of a discharge pulse that satisfies the condition $P_i^{\pm}(E_c)\Delta t \ll 1$.

The third assumption above implies that the drop in local surface field due to the ith PD event can be expressed as

$$\Delta E_i^{\pm} = \kappa q_i^{\pm}, \tag{21}$$

where κ is a constant.

From assumption (4) and (5), the local surface field strength at any given time is given by

$$E(t) = E_o \sin\omega t - \sum_{j=1}^{N} \Delta E_{ij}^{\pm}(\phi_{ij}^{\pm}), \tag{22}$$

where $\Delta E_{ij}^{\pm}$ is the field drop due to the ith PD pulse in the jth voltage cycle and N is number of cycles that have occurred up to time t. The phase-of-occurrence, $\phi_{ij}^{\pm}$, of the ith PD pulse is defined to lie in the interval $(0, 2\pi)$. Thus the time, t_{ij}, at which the ith pulse occurred in the jth cycle is given by

$$t_{ij} = \left(\frac{\phi_{ij}}{2\pi} + j - 1\right) T, \tag{23}$$

where $t_{ij} < t$.

2.3.3 Stochastic Analysis of Simulation

The theoretical model described in the previous section has been used as the basis for developing a computer program that generates a continuous sequence of random phase-correlated pulses that mimic the observed behavior of ac-generated

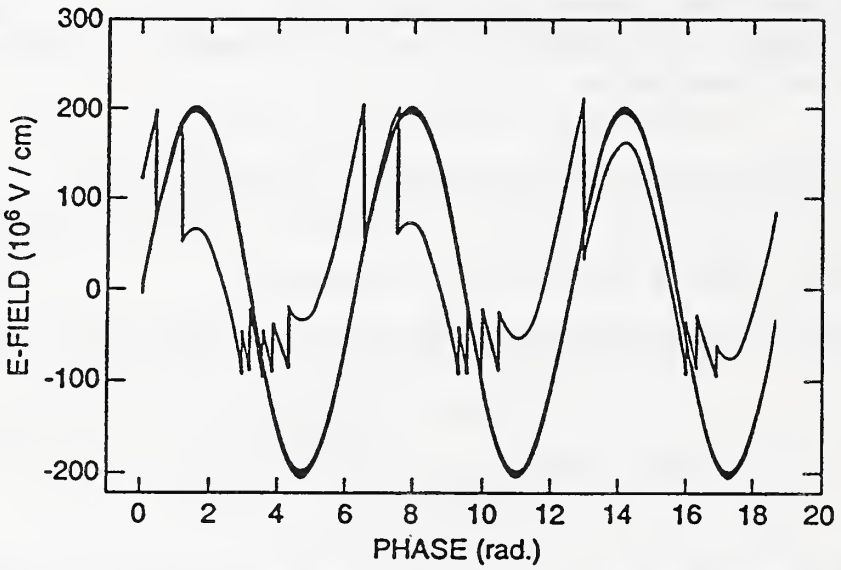

Figure 10. Three randomly selected cycles from a Monte-Carlo PD simulation. Shown is the applied sinusoidal field (thick line) and the local field given by eq (22) (thin line).

PD phenomena. Figure 10 shows a plot of the local field as determined by eq (22) for three randomly selected cycles together with the applied field. These data were obtained under the same conditions that apply to the results shown in the next section. The corresponding pulse amplitudes were determined from eq (21) for $\kappa = 1$.

As successive pulses are generated by the simulation, their phases and amplitudes are accumulated by the computer into "bins" used to determine a set of various conditional and unconditional probability distributions in "real time". The computer software routine that controls this sorting of pulses is described elsewhere [71].

The distributions determined for the particular case considered in this report include: $p_0(\phi_i^{\pm})$, $p_1(\phi_i^{\pm} \mid Q^{\mp})$, and $p_2(q_i^{\pm} \mid \phi_i^{\pm}, Q^{\mp})$ as defined in previous work [63, 65, 71]. Here $Q^{\pm}$ is the sum of all positive or negative pulse amplitudes for a particular half-cycle, i.e.,

$$Q^{\pm} = \sum_i q_i^{\pm}. \tag{24}$$

The distributions are defined such that, for example, $p_0(\phi_i^-)d\phi_i^-$ is the probability that the ith negative pulse in a cycle has a phase-of-occurrence between ϕ_i^- and $\phi_i^- + d\phi_i^-$; $p_1(\phi_i^- \mid Q^+)d\phi_i^-$ is the probability that it will have a phase-of-occurrence in this range if Q^+ for the previous half-cycle has a "fixed" value, and $p_2(q_i^- \mid Q^+, \phi_i^-)dq_i^-$ is the probability that the ith negative pulse has an amplitude between q_i^- + dq_i^- if both Q^+ and its phase, ϕ_i^-, are fixed. The fixed variables are specified to lie within narrow ranges. The conditional distributions provide a direct indication of memory effects. If, for example, it is found that $p_0(\phi_i^-) \neq p_1(\phi_i^- \mid Q^+)$ for at least some value of Q^+, then it can be stated that the most probable phase-of-occurrence for the ith negative

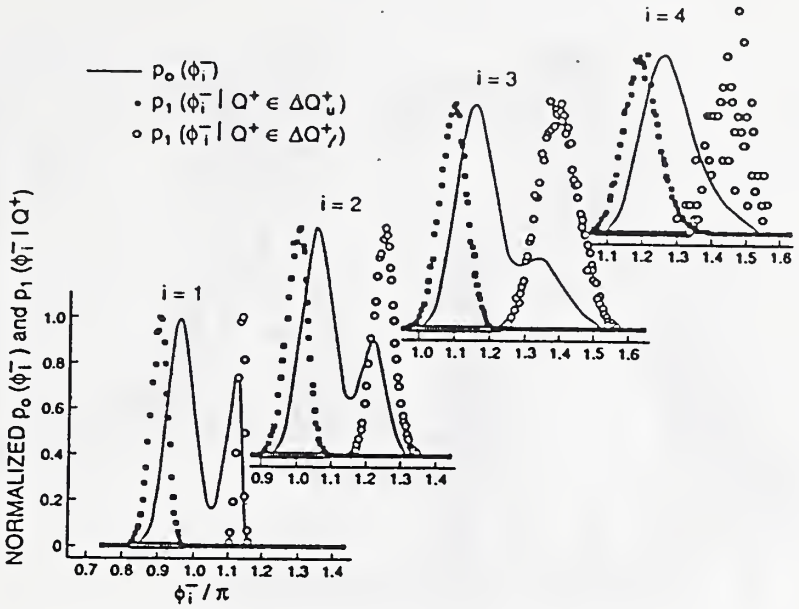

Figure 11. Unconditional (lines) and conditional (points) phase-of-occurrence distributions for the first, second, third, and fourth negative PD pulses. All distributions have been normalized to the maximum value.

pulse depends on the total charge, Q^+, associated with all PD events on the previous half-cycle. (Note that the amplitude of a PD is conventionally expressed in units of charge [63, 65]).

2.3.4 Results and Discussion

To obtain the results shown here, the simulation was performed using the values $E_0 = 2 \times 10^8$ V/cm, $\Phi_+ = 0.95\,\text{eV}$, $\Phi_- = 0.57\,\text{eV}$, $E_I^+ = 8.74 \times 10^7$ V/cm, $E_I^- = -3.87 \times 10^7$ V/cm. Data were accumulated for 10^6 cycles using 10^3 time increments, Δt, per cycle. The simulated PD under these conditions produce an asymmetric pattern in which one or two large pulses appear on the positive half-cycle and three to seven smaller pulses typically appear on the negative half-cycle (see Fig. 10). This behavior is similar to that seen in some point-dielectric discharge gaps [64, 68].

Results for unconditional and conditional phase-of-occurrence distributions $p_0(\phi_i^-), p_1(\phi_i^- \mid Q^+)$, $i = 1, 2, 3, 4$ and $p_0(\phi_i^+), p_1(\phi_i^+ \mid Q^-), i = 1, 2$ are shown respectively in Figures 11 and 12. The corresponding integrated charge distributions $p_0(Q^+)$ and $p_0(Q^-)$ are shown in Fig. 13. The windows that specify the upper and lower fixed value ranges for Q^+ and Q^- used to obtain the conditional distributions shown in Figs. 11 and 12 are also indicated in Fig. 13. It is evident from the conditional distributions that the larger the absolute value of $Q^\mp$ the lower is the phase $\phi_i^\pm$ at which pulses occur on the subsequent half-cycle. This behavior is consistent with

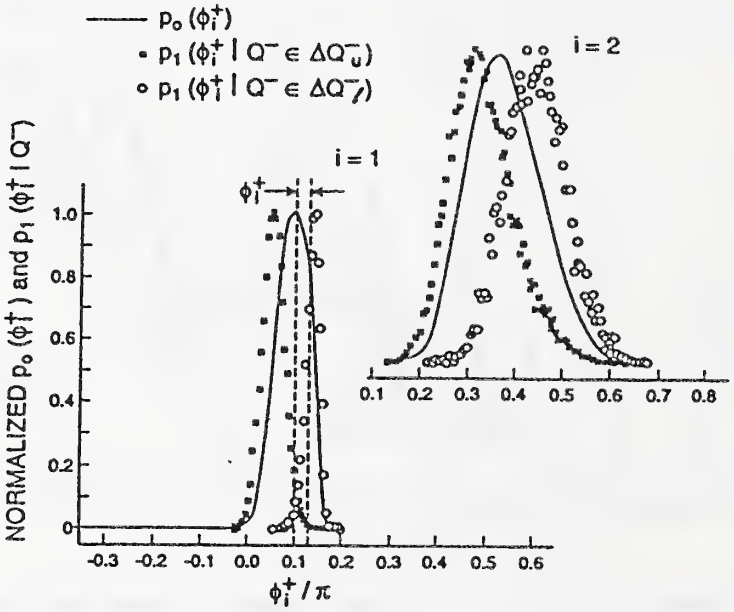

Figure 12. Unconditional (lines) and conditional (points) phase-of-occurrence distributions for the first and second positive PD pulses. Indicated by the vertical lines is the phase window used to specify ϕ_1^+ for the second-order conditional pulse-amplitude distribution shown in Fig. 13. All distributions have been normalized to the maximum value.

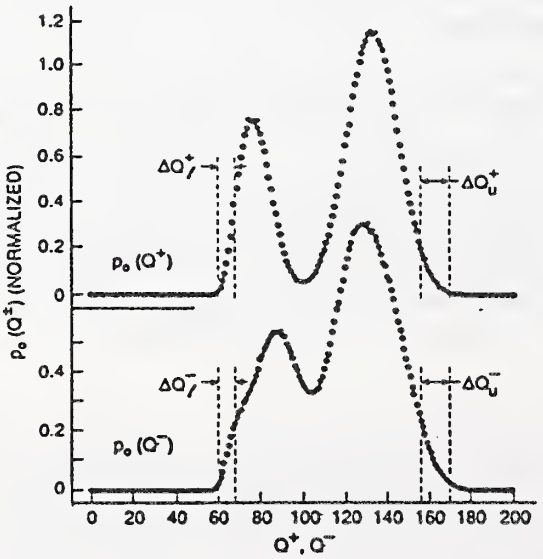

Figure 13. Integrated charge distributions for positive and negative pulses. The vertical lines indicate the windows used to specify the Q^+ and Q^- values for determination of the conditional distributions in Figures 11, 12, and 14.

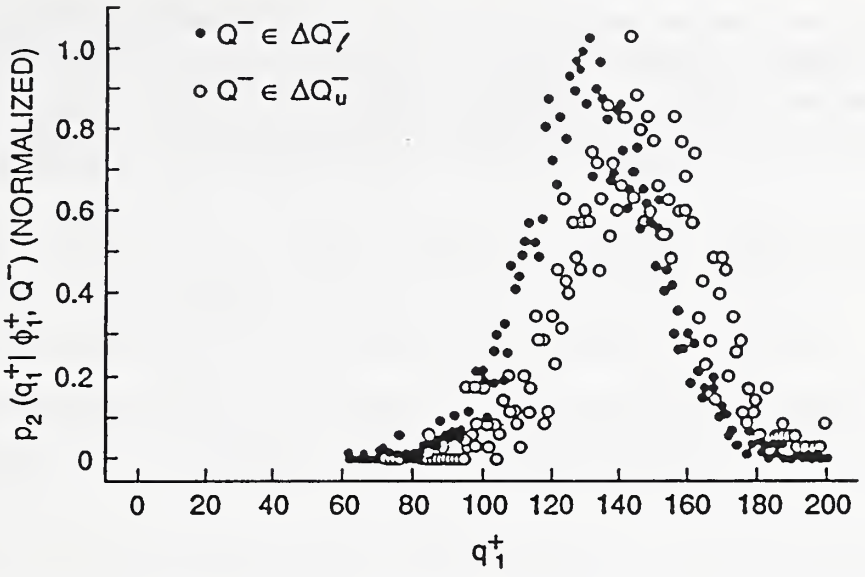

Figure 14. Second-order conditional amplitude distribution for the first positive PD pulse. The charge windows are defined in Fig. 13.

experimental results [64, 65, 68] and clearly demonstrates the existence of significant memory propagation.

It was determined that the bimodal structure in $p_0(Q^+)$ is due primarily to the difference in total charge on the positive half-cycle resulting from one and two discharge events. This characteristic has also been seen in experimental results [71]. Because the distribution functions shown in Figures 11–13 are not independent when memory is important, the bimodal structure originating in $p_0(Q^+)$ can also be reflected in the other unconditional distributions such as $p_0(\phi_1^-)$. The distributions $p_0(\phi_i^-), p_1(\phi_i^- \mid Q^+)$, and $p_0(Q^+)$ are related, according to the law of probabilities, by the integral expression

$$p_0(\phi_i^-) = \int_0^\infty p_0(Q^+) p_1(\phi_i^- \mid Q^+) dQ^+. \tag{25}$$

Bimodal structure in the PD phase distributions has also been seen in experimental results [68].

The second-order conditional distribution $p_2(q_1^+ \mid \phi_1^+, Q^-)$ for the first positive PD pulse is shown in Figure 14. The appropriate windows for ϕ_1^+ and Q^- are those indicated respectively in Figures 12 and 13. Again, consistent with experimental results [65], it is seen that the larger the absolute value for Q^- in the previous half-cycle, the larger will be the value of the amplitude for the first positive pulse that occurs at a particular phase in the next half-cycle.

It has thus been demonstrated from the results presented here that it is possible, using reasonable assumptions, to simulate PD patterns that have the same stochastic

properties as those observed experimentally. Tests of the stochastic behavior are essential in validating theoretical models of pulsating PD phenomena. Simulated PD pulses may also prove useful in testing the performance of systems used to measure stochastic behavior, e.g., conditional pulse-amplitude and phase distributions [71].

3. REFERENCES

[1] N. Wertheimer and E. Leeper, *Am. J. Epidemiol.* **109**, 273 (1979).

[2] D.A. Savitz and E.E. Calle, *J. Occup. Med.* **29**, 47 (1987).

[3] Abstracts W1-W7, First World Congress for Electricity and Magnetism in Biology and Medicine, Lake Buena Vista, FL, pp. 65–67 (1992).

[4] D.L. Mader and S.B Peralta, Bioelectromagnetics **13**, 287, (1992).

[5] IEEE Magnetic Fields Task Force, "A Protocol for Spot Measurements of Residential Power Frequency Magnetic Fields," *IEEE Trans. Power Delivery*, in press.

[6] J.R. Gauger, *IEEE Trans. Power Appar. Syst.* **PAS-104**, 2436 (1985).

[7] D. Corson and P. Lorrain, Introduction to Electromagnetic Fields and Waves, W.H. Freeman, San Francisco, CA (1962), p. 210.

[8] K.R. Symon, Mechanics, Addison-Wesley, Reading, MA (1953), p. 83.

[9] G.B. Thomas, Calculus and Analytic Geometry, Addison-Wesley, Reading, MA (1953), pp. 497–500.

[10] G.B. Thomas, Calculus and Analytic Geometry, Addison-Wesley, Reading, MA (1953), pp. 550–553.

[11] C.R.C. Standard Mathematical Tables, Eleventh Edition, Hodgman, C.D. (Ed.), Chemical Rubber Publ. Co., Cleveland, OH.

[12] IEEE Electromagnetic Compatibility Society, draft 9, "Standard Procedures for the Measurement of Electric and Magnetic Fields from Video Display Terminals (VDTs) from 5 Hz to 400 kHz," July, 1992.

[13] M. Misakian, "Coil Probe Dimensions and Uncertainties During Measurements of Nonuniform ELF Magnetic Fields," submitted to *NIST Journal of Research.*

[14] D.R. James, I. Sauers, G.D. Griffin, R.J. Van Brunt, J.K. Olthoff, K.L. Stricklett, F.Y. Chu, J.R. Robins, and H.D. Morrison, *Elect. Insul. Magazine*, **9**, 29 (1993).

[15] J.K. Olthoff, R.J. Van Brunt, J.T. Herron, and I. Sauers, *Anal. Chem.* **63**, 726 (1991).

[16] I. Sauers and R.A. Cacheiro, *Conference Record 1992 IEEE International Symposium on Electrical Insulation*, IEEE, New York, pp. 340–344 (1992).

[17] R.J. Van Brunt, J.K. Olthoff, I. Sauers, H.D. Morrison, J.R. Robins, and F.Y. Chu, *Proc. 10th Int. Conf. on Gas Discharges and their Applications*, University College of Swansea, UK, pp. 418–421 (1992).

[18] R.J. Van Brunt, J.K. Olthoff, and M. Shah, *Conference Record of the 1992 IEEE International Symposium on Electrical Insulation*, IEEE, New York, pp. 328–331 (1992).

[19] H.-X. Wan, J.H. Moore, J.K. Olthoff, and R.J. Van Brunt, *Plasma Chem. Plasma Proc.* **13**, 1 (1993).

[20] J.K. Olthoff, K.L. Stricklett, R.J. Van Brunt, J.H. Moore, J.A. Tossell, and I. Sauers, *J. Chem. Phys.* **98**, 9466 (1993).

[21] R.J. Van Brunt and E.W Cernyar, 1992 Annual Report - *Conference on Electrical Insulation and Dielectric Phenomena*, IEEE, New York, pp. 427–434 (1992).

[22] K.G. Denbigh and R. Whytlaw-Gray, *J. Chem. Soc.* 1346 (1934).

[23] J. Czarnowski and H.J. Schumacher, *Int. J. Chem. Kinetics* **11**, 614 (1979).

[24] C.J. Merrill and G.H. Cady, *J. Am. Chem. Soc.* **83**, 298 (1961).

[25] J.T. Herron, *Int. J. Chem. Kinetics* **19**, 129 (1987).

[26] S.W. Benson and J. Bott, *Int. J. Chem. Kinetics* **1**, 451 (1969).

[27] W.R. Trost and R.L. McIntosh, *Can. J. Chem.* **29**, 508 (1952).

[28] A.C. Gonzlez and H.J. Schumacher, Z. Naturforsch. **36B**, 1381 (1981).

[29] S.K. Bains-Sahota and M.H. Thiemens, *J. Chem. Phys.* **90**, 6099 (1989).

[30] R.J. Van Brunt and J.T. Herron, *IEEE Trans. Elec. Insul.* **25**, 75 (1990).

[31] I. Sauers, P.C. Votaw, and G.D. Griffin, *J. Phys. D* **21**, 1236 (1988).

[32] W. Becher and J. Massonne, ETZ-A **91**, 605 (1970).

[33] G.D. Griffin, M.G. Nolan, I. Sauers, K. Kurka, M.D. Morris, and P.C. Votaw, In Vitro **25**, 673 (1989).

[34] F.J.J.G. Janssen, Kema Sci. Technol. Rep. **2**, 9 (1984); *Gaseous Dielectrics V*, Pergamon Press, New York, pp. 153-162 (1986).

[35] R.B. Harvey and S.H. Bauer, *J. Am. Chem. Soc.* **76**, 859 (1954).

[36] G.L. Gutsev, *Chem. Phys.* **158**, 33 (1991).

[37] H. Oberhammer and K. Seppelt, *Inorg. Chem.* **17**, 1435 (1978).

[38] P. Zylka, H. Oberhammer, and K. Seppelt, *J. Molec. Structure* **243**, 411 (1991).

[39] B. Cohen and A.G. MacDiarmid, *Inorg. Chem.* **1**, 754 (1962).

[40] J.K. Olthoff, R.J. Van Brunt, and I. Sauers, *J. Phys. D* **22**, 1399 (1989).

[41] I. Sauers, L.G. Christophorou, and S.M. Spyrou, *Plasma Chem. Plasma Proc.*, **13**, 17 (1993).

[42] A. Stamatovic and G.J. Schulz, *Rev. Sci. Instrum.* **41**, 423 (1970); M.R. McMillan and J.H. Moore, *Rev. Sci. Instrum.* **51**, 944 (1980); G. J. Schulz, *Phys. Rev. A* **5**, 1672 (1972).

[43] H.-X. Wan, J.H. Moore, and J.A. Tossell, *J. Chem. Phys.* **91**, 7340 (1989); **94**, 1868 (1991).

[44] G.J. Schulz, *Rev. Mod. Phys.* **45**, 423 (1973).

[45] A.R. Johnston and P.D. Burrow, *J. Electron Spectrosc. Relat. Phenom.* **25**, 119 (1982).

[46] A. Hadjiantoniou, L.G. Christophorou, and J.G. Carter, *J. Chem. Soc. Faraday Trans. II* **69**, 1691 (1973).

[47] S.M. Spyrou, I. Sauers, and L.G. Christophorou, *J. Chem. Phys.* **78**, 7200 (1983).

[48] L.E. Kline, D.K. Davies, C.L. Chen, and P.J. Chantry, *J. Appl. Phys.* **50**, 6789 (1979).

[49] L.W. Sieck and R.J. Van Brunt, *J. Phys. Chem.* **92**, 708 (1988).

[50] E.P. Wigner, *Phys. Rev.* **73**, 1002 (1948).

[51] A. Chutjian and S.H. Alajajian, *Phys. Rev. A* **31**, 2885 (1985); O.J. Orient and A. Chutjian, *Phys. Rev. A* **34**, 34 (1986); S.H. Alajajian and A. Chutjian, *J. Phys. B* **20**, 2117 (1987).

[52] D. Klar, M.-W. Ruf, and H. Hotop, *Aust. J. Phys.* **45**, 263 (1992).

[53] T. Ziegler and G.L. Gutsev, *J. Chem. Phys.* **96**, 7623 (1992).

[54] R.N. Compton, P.W. Reinhardt, C.D. Cooper, *J. Chem. Phys.* **68**, 2023 (1978).

[55] P.W. Harland and J.C.J. Thynne, *J. Phys. Chem.* **75**, 3517 (1971); J. E. Delmore and A. D. Appelhans, *J. Chem. Phys.* **84**, 6238 (1986).

[56] J.A. Tossell, *Chem. Phys.* **154**, 211 (1991).

[57] J.J.P. Stewart, J. Computer-Aided Molec. Design **4**, 1 (1990).

[58] M.W. Schmidt, J.A. Boatz, K.K. Baldridge, S. Koseki, M.S. Gordon, S.T. Elbert, and B. Lam, QCPE Bull. **7**, 115 (1987).

[59] J.S.-Y. Chao and K.D. Jordan, *J. Phys. Chem.* **91**, 5578 (1987).

[60] R.E. Kennerly, R.A. Bonham, and M. McMillian, *J. Chem. Phys.* **70**, 2039 (1979).

[61] G.E. Streit, *J. Chem. Phys.* **77**, 826 (1982).

[62] P.J. Hay, *J. Chem. Phys.* **76**, 512 (1982).

[63] R. J. Van Brunt and S. V. Kulkarni, *Phys. Rev. A* **42**, 4908 (1990).

[64] R. J. Van Brunt and E. W. Cernyar, *Appl. Phys. Lett.* **58**, 2628 (1991).

[65] R. J. Van Brunt, *IEEE Trans. Elect. Insul.* **26**, 902 (1991).

[66] A. I. Bennett, "Endurance of Electrical Insulation Under Sinusoidal Voltage Stress," Annual Report of the CEIDP, IEEE, NY pp. 80–88 (1987).

[67] F. Fruth and L. Niemeyer, *IEEE Trans. Elect. Insul.* **27**, 60 (1992).

[68] R. J. Van Brunt, E. W. Cernyar, P. von Glahn, and T. Las, *Conf. Rec. 1992 IEEE Int. Symp. on Elect. Insul.*, IEEE, NY, pp. 349–353 (1992).

[69] R. H. Fowler and L. Nordheim, *Proc. Roy. Soc. London, Ser. A* **119**, 173 (1928).

[70] R. V. Latham, H. V. "Vacuum Insulation-Physical Basis", Academic Press, NY, pp. 51–79 (1981).

[71] R. J. Van Brunt and E. W. Cernyar, *NIST J. Res.* **92**, 635 (1992).